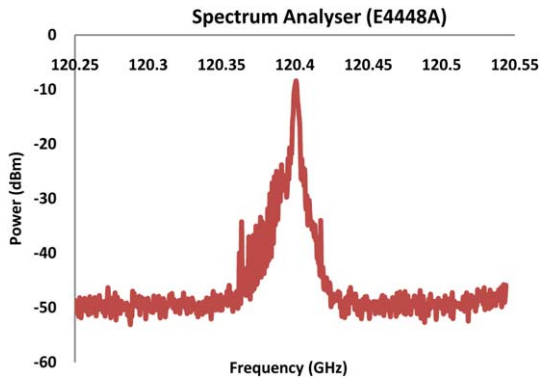

Figure 5 Spectrum analyzer measurement for second harmonics frequency using W-band setup. [Color figure can be viewed in the online issue, which is available at wileyonlinelibrary.com]

4. CONCLUSIONS AND DISCUSSION

The letter describes an AlGaAs/GaAs-based planar Gunn diode fabricated on a GaAs semi-insulating substrate with an integrated series inductor to resonate out the diode capacitance at high frequency. RF measurements have been presented in which a device with a 1 μm active channel length oscillated with a fundamental frequency of 120.47 GHz and an RF output power of -9.14 dBm, which is the highest reported fundamental frequency and output power from a GaAs-based Gunn diode.

ACKNOWLEDGMENTS

The authors thank the staff of the James Watt Nanofabrication Centre at the University of Glasgow for help in fabricating the devices reported in this paper and also we thank Mr. Krishna Nama for his support in SEM measurements. Part of this work was supported by ESPRC through EP/H011366/1 and EP/H012966/1.

REFERENCES

1. P.H. Siegel, Terahertz technology, IEEE Trans Microwave Theory Tech 50 (2002), 910–928.
2. T.W. Crowe, D.W. Porterfield, J.L. Hesler, W.L. Bishop, D.S. Kurtz, and K. Hui, Terahertz sources and detectors, 2005, pp. 271–280.
3. X. Yin, B.W.-H. Ng, and D. Abbott, Terahertz imaging for biomedical applications, Springer, New York, NY, 2012, pp. 9–27.
4. S.J.J. Teng and R.E. Goldwasser, High-performance second-harmonic operation W-band GaAs Gunn diodes, IEEE Electron Device Lett 10 (1989), 412–414.
5. L. Varani, C. Palermo, J.F. Millithaler, J.C. Vaissière, E. Starikov, P. Shiktorov, V. Gružinskis, J. Mateos, S. Pérez, D. Pardo, and T. González, Numerical modeling of TeraHertz electronic devices, J Comput Electron 5 (2006), 71–77.
6. Y.P. Teoh, G.M. Dunn, N. Priestley, and M. Carr, Monte Carlo simulations of asymmetry multiple transit region Gunn diodes, Semicond Sci Technol 20 (2005), 418–422.
7. A. Khalid, N.J. Pilgrim, G.M. Dunn, M.C. Holland, C.R. Stanley, I.G. Thayne, and D.R.S. Cumming, A planar Gunn diode operating above 100 GHz, IEEE Electron Device Lett 28 (2007), 849–851.
8. C. Li, Millimeter-wave planar Gunn diodes and integrated circuits, University of Glasgow, 2011.
9. M.I. Maricar, J. Glover, G. Evans, V. Papageorgiou, D. Cumming, and C. Oxley, Planar Gunn diode and resonators, In: 4th Annual Seminar on Passive RF and Microwave Components, 2013, pp. 2–5.
10. A. Khalid, C. Li, V. Papageogiou, G.M. Dunn, M.J. Steer, I.G. Thayne, M. Kuball, C.H. Oxley, M. Montes Bajo, A. Stephen, J. Glover, and D.R.S. Cumming, In0.53Ga0.47As planar Gunn diodes operating at a fundamental frequency of 164 GHz, Electron Device Lett IEEE 34 (2013), 39–41.
11. C. Li, A. Khalid, N. Pilgrim, M.C. Holland, G. Dunn, and D.S.R. Cumming, Novel planar Gunn diode operating in fundamental mode up to 158 GHz, J Phys Conf Ser 193 (2009), 012029.
12. A. Khalid, C. Li, V. Papageorgiou, N.J. Pilgrim, G.M. Dunn, and D.R.S. Cumming, A 218-GHz second-harmonic multiquantum well GaAs-based planar Gunn diodes, Microwave Opt Technol Lett 55 (2013), 686–688.
13. C. Li, A. Khalid, L.B. Lok, N.J. Pilgrim, M.H. Holland, G.M. Dunn, and D.R.S. Cumming, Millimeter-wave planar Gunn diodes, In: Unknown Conference in Sheffield, 2010.
14. W.H. Haydl, Planar Gunn diodes with ideal contact geometry, IEEE Electron Device Lett 61 (1972), 1972.
15. M.I. Maricar, J. Glover, G.A. Evans, A. Khalid, V. Papageorgiou, L. Chong, G. Dunn, and C.H. Oxley, Planar Gunn diode characterisation and resonator elements to realise oscillator circuits, In: International Conference on Advanced Nanomaterials & Emerging Engineering Technologies, ICANMEET-2013, 2013, pp. 674–678.

ADAPTIVE GROUPING FOR THE HIGHER-ORDER MULTILEVEL FAST MULTIPOLE METHOD

Oscar Borries,[1,2] Erik Jørgensen,[1] Peter Meincke,[1] and Per Christian Hansen[2]
[1] TICRA, DK-1201, Copenhagen, Denmark
[2] Department of Applied Mathematics and Computer Science, Technical University of Denmark, DK-2800, Kgs. Lyngby, Denmark; Corresponding author: ob@ticra.com

Received 4 March 2014

ABSTRACT*An alternative parameter-free adaptive approach for the grouping of the basis function patterns in the multilevel fast multipole method is presented, yielding significant memory savings compared to the traditional Octree grouping for most discretizations, particularly when using higher-order basis functions. Results from both a uniformly and nonuniformly meshed scatterer are presented, showing how the technique is worthwhile even for regular meshes, and demonstrating that there is no loss of accuracy in spite of the large reduction in memory requirements and the relatively low computational cost.* © 2014 Wiley Periodicals, Inc. Microwave Opt Technol Lett 56:2451–2456, 2014; View this article online at wileyonlinelibrary.com. DOI 10.1002/mop.28611

Key words: *MLFMM; higher-order discretization; irregular meshes*

1. INTRODUCTION

When solving large-scale electromagnetic scattering problems, where the unknown is the surface current density induced by an incident electromagnetic field on a scatterer, the multilevel fast multipole method (MLFMM) [1–4] is one of the most powerful methods for speeding up the necessary matrix-vector products involved in an iterative solution.

The MLFMM is a hierarchical algorithm which achieves an asymptotic complexity of $\mathcal{O}(N\log N)$, N being the number of unknowns, by computing interactions between groups of basis functions rather than individual basis functions. The multilevel aspect comes from using a hierarchical grouping to allow interactions over increasing distances to be done by considering increasingly larger groups.

The first step of the MLFMM is the application of a grouping algorithm. The grouping effectively determines the region of validity of the Green's function expansion underlying the MLFMM. Furthermore, the grouping dictates the number of terms needed to represent the functions involved in MLFMM,

often called the *bandwidth*, and therefore also the required number of samples of those functions on the unit sphere, called the *sampling rate*. In most implementations [2,4], this grouping is done using the Octree algorithm [5]. This is a fast, easily implemented and conceptually simple algorithm, designed in computer graphics to adapt very well to any geometrical shape. In the context of the MLFMM, it also has the extremely important feature of allowing reuse of some of the quantities involved [6].

However, as the discretizations become more irregular, which is often the case for higher-order discretizations applied to realistic problems, the Octree grouping at the finest level results in excessive sampling rates. This is due to the Octree only considering the center of the geometrical elements, known as patches, as well as the size of the largest patch, rather than taking into account the size and shape of the individual patch. To reduce the memory consumption significantly, particularly for very irregular meshes or for meshes with large patches, we suggest in this article a grouping method that allows the grouping on the finest level to become completely adaptive to the shape of the patches. The method results in a modest increase in the computational cost of a matrix-vector product, which will be discussed in Section 4. Although this method is conceptually simple, it has not to our knowledge been published previously.

The time factor $e^{j\omega t}$, where ω is the angular frequency, is assumed and suppressed throughout.

2. MULTILEVEL FAST MULTIPOLE METHOD

In the present article, the MLFMM is used when solving the electric field integral equation (EFIE) [7]

$$\hat{\boldsymbol{n}}\times\boldsymbol{E}^i=\mathcal{L}\boldsymbol{J}_{\mathcal{S}}, \tag{1}$$

using an iterative solver. In (1), $\hat{\boldsymbol{n}}$ is a unit vector normal to the scatterer $\mathcal{S}$, $\boldsymbol{E}^i$ is the incident electric field, and $\boldsymbol{J}_{\mathcal{S}}$ is the unknown surface current density. Further, $\mathcal{L}$ is the integral operator

$$\mathcal{L}\boldsymbol{J}_{\mathcal{S}}=\hat{\boldsymbol{n}}\times j\omega\mu\left[\int_{\mathcal{S}}\boldsymbol{J}_{\mathcal{S}}(\boldsymbol{r}')G(\boldsymbol{r},\boldsymbol{r}')d^2\boldsymbol{r}'+\frac{1}{k^2}\int_{\mathcal{S}}\nabla'_{\mathcal{S}}\cdot\boldsymbol{J}_{\mathcal{S}}(\boldsymbol{r}')\nabla G(\boldsymbol{r},\boldsymbol{r}')d^2\boldsymbol{r}'\right], \tag{2}$$

where μ is the free-space permeability, $k=2\pi/\lambda$, with λ being the free-space wavelength. $G(\boldsymbol{r},\boldsymbol{r}')=\frac{e^{-jk|\boldsymbol{r}-\boldsymbol{r}'|}}{4\pi|\boldsymbol{r}-\boldsymbol{r}'|}$ is the free-space Green's function and $\boldsymbol{r},\boldsymbol{r}'$ denote observation and integration points, respectively. For some scenarios, it is more useful to apply the combined field integral equation (CFIE) [7],

$$\left[\alpha\mathcal{L}+(1-\alpha)\eta\left(\frac{1}{2}\mathcal{I}+\mathcal{K}\right)\right]\boldsymbol{J}_{\mathcal{S}}=\alpha\hat{\boldsymbol{n}}\times\boldsymbol{E}^i+(1-\alpha)\eta\hat{\boldsymbol{n}}\times\boldsymbol{H}^i. \tag{3}$$

where $\mathcal{I}$ is the identity operator, $\boldsymbol{H}^i$ is the incident magnetic field, η is the free-space impedance, $\alpha\in[0,1]$ is a weighting factor, and $\mathcal{K}$ is the operator

$$\mathcal{K}\boldsymbol{J}_{\mathcal{S}}=\hat{\boldsymbol{n}}\times-\int_{\mathcal{S}}\boldsymbol{J}_{\mathcal{S}}(\boldsymbol{r}')\times\nabla G(\boldsymbol{r},\boldsymbol{r}')d^2\boldsymbol{r}', \tag{4}$$

where $-\int$ denotes the Cauchy principal value.

The central part of the MLFMM is Rokhlin's translator [1]

$$T_L(k,\hat{\boldsymbol{k}},\boldsymbol{x})=\sum_{l=0}^{L}(-j)^l(2l+1)h_l^{(2)}(k\|\boldsymbol{x}\|_2)P_l(\hat{\boldsymbol{k}}\cdot\hat{\boldsymbol{x}}), \tag{5}$$

where $\hat{\boldsymbol{k}}$ is the unit wave vector, $\boldsymbol{x}$ is the vector between two group centers, $\hat{\boldsymbol{x}}=\boldsymbol{x}/\|\boldsymbol{x}\|_2$, $h_l^{(2)}$ is the spherical Hankel function of second kind and order l, and P_l is the Legendre polynomial of degree l. It is important to note that the translator does not depend on the absolute position of the groups, but only on the vector $\boldsymbol{x}$ between their centers. Thus, the translator can be reused for pairs of groups with the same $\boldsymbol{x}$, a key factor in keeping memory consumption low. Typically, the number of terms $L+1$ in the translator is determined from the excess bandwidth formula [8]

$$L=kD+1.8\beta^{2/3}(kD)^{1/3}, \tag{6}$$

where $D=\sqrt{3}a$ is the diameter of the group, a is the sidelength of the group, and $10^{-\beta}$ is the desired relative error.

To discretize the problem, we begin by representing the surface of the scatterer $\mathcal{S}$ by geometric elements known as patches. Then, (1) is discretized using a Galerkin method to yield a linear system $\overline{\overline{Z}}\overline{I}=\overline{B}$. Here, $\overline{I}$ is a vector containing coefficients to the basis functions expressing the surface current density, $\overline{\overline{Z}}$ is a matrix containing as its (i,j)'th component the mutual impedance between basis functions $\boldsymbol{f}_i$ and $\boldsymbol{f}_j$, and $\overline{B}$ is a vector, representing the incident field as tested by the basis functions [9]. We can consider MLFMM as a method for splitting the matrix $\overline{\overline{Z}}$ into two parts

$$\overline{\overline{Z}}=\overline{\overline{Z}}_{\text{near}}+\overline{\overline{Z}}_{\text{far}}, \tag{7}$$

where the *near-matrix* $\overline{\overline{Z}}_{\text{near}}$ is stored as a sparse matrix, while $\overline{\overline{Z}}_{\text{far}}$ is not stored directly, but instead the elements required to multiply $\overline{\overline{Z}}_{\text{far}}$ with an excitation vector $\overrightarrow{I}$ are stored.

Introducing the basis function patterns as

$$\boldsymbol{V}_{jm}(k,\hat{\boldsymbol{k}})=\int_{\mathcal{S}}\boldsymbol{f}_j(\boldsymbol{r})\cdot[\overline{\overline{I}}-\hat{\boldsymbol{k}}\hat{\boldsymbol{k}}]e^{-jk\hat{\boldsymbol{k}}\cdot(\boldsymbol{r}_m-\boldsymbol{r})}d^2\boldsymbol{r}, \tag{8}$$

where $\overline{\overline{I}}$ is the identity matrix, and utilizing (5), we can express the matrix elements resulting from the EFIE (1) as

$$\overline{\overline{Z}}_{\text{far}\,(j,i)}=\oint\!\!\!\!\!\!S\,\boldsymbol{V}_{jm}^*(k,\hat{\boldsymbol{k}})\cdot\left(T_L(k,\hat{\boldsymbol{k}},\boldsymbol{r}_{mm'})\boldsymbol{V}_{im'}(k,\hat{\boldsymbol{k}})\right)d^2\hat{\boldsymbol{k}}, \tag{9}$$

which is then discretized to

$$\overline{\overline{Z}}_{\text{far}\,(j,i)}=\kappa\sum_{p=1}^{K}w_p\boldsymbol{V}_{jm}^*(k,\hat{\boldsymbol{k}}_p)\cdot\left(T_L(k,\hat{\boldsymbol{k}}_p,\boldsymbol{r}_{mm'})\boldsymbol{V}_{im'}(k,\hat{\boldsymbol{k}}_p)\right), \tag{10}$$

where κ is a constant depending on the units of the impedance matrix $\overline{\overline{Z}}$, $K=2(L+1)^2$ is the number of sample points on the unit sphere [10], and w_p are the integration weights. We assume that $\boldsymbol{f}_i$ belongs to group m' and $\boldsymbol{f}_j$ belongs to group m, $\boldsymbol{r}_{mm'}=\boldsymbol{r}_m-\boldsymbol{r}_{m'}$ where $\boldsymbol{r}_m$ denotes the center of group m, and we further assume that $|\boldsymbol{r}_{mm'}|>D$. If $|\boldsymbol{r}_{mm'}|\leq D$, the element $\overline{\overline{Z}}_{j,i}$ must be computed directly and stored in $\overline{\overline{Z}}_{\text{near}}$. For the CFIE (3), the expression for the matrix elements corresponding to (10) are slightly more complicated [4].

The key issue from (8) and (10) is that the number of sample points for the basis function patterns $\boldsymbol{V}_{jm}$ is the same as that required for the translator, even though the bandwidth of $\boldsymbol{V}_{jm}$ is

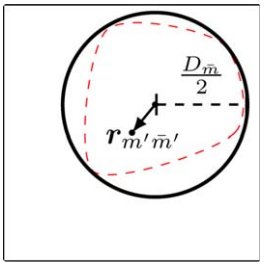

Figure 1 2-D illustration of adaptive grouping. The dashed line is the projection of a patch onto a plane, while the square is the box at the finest level of the Octree. To the left is shown the scenario obtained with using the Octree grouping at the finest level as a foundation for the basis function patterns. Further subpartitioning would dissect the patch, which is suboptimal. Instead, on the right, we introduce an adaptive grouping layer, which has its center such as to minimize the size of the circle enclosing the patch. We thus see that the region of validity, indicated by the solid black circle, is much smaller than it would be if it had to enclose the entire square. The $\boldsymbol{r}_{m'\bar{m}'}$ vector indicates the phase-center shift needed to start the upward pass. [Color figure can be viewed in the online issue, which is available at wileyonlinelibrary.com]

lower [10]. Note that the bandwidth of $\boldsymbol{V}_{jm}$ is directly related to the largest value of $|\boldsymbol{r}_m - \boldsymbol{r}|$ attained on the domain of $\boldsymbol{f}_j$, due to the term $e^{-jk\hat{\boldsymbol{k}}\cdot(\boldsymbol{r}_m-\boldsymbol{r})}$ in (8).

3. GROUPING

An Octree [5] is used here as a hierarchical data structure, allowing a geometrical object to be spatially partitioned in a fast and simple manner, thereby providing a grouping of basis functions that are spatially near each other. The Octree grouping is done by creating an original bounding box for $\mathcal{S}$, hereafter termed level 1 or the coarsest level. Finer levels are then created by partitioning boxes such that the diameter of the boxes at level q is $D_q = D_{q-1}/2$. This results in eight potential boxes per partitioning, of which only those that contain the center of a patch are kept while the rest are pruned. This results in a very fast partitioning of the patches into clusters. The partitioning stops when

$$D_q/2 < l, \tag{11}$$

where l is the largest sidelength of any patch in the mesh surface, yielding q levels in the Octree.

However, as Figure 1 illustrates, this will occasionally result in unnecessarily large groups at the finest level, simply because the Octree scheme is not able to adapt to the patches. Effectively, the center point for $\boldsymbol{V}_{jm}, \boldsymbol{r}_m$, is positioned such that the sample rate will be far too large. The memory cost for this can be very significant. Further, as the sampling rate for all boxes at each level is the same, and as the finest level box size is determined by the largest patch length in the mesh, scenarios with nonuniform patch sizes will result in far too large sampling rates for the groups with smaller patches.

Therefore, we propose to tabulate each $\boldsymbol{V}_{jm}$ based on a separate *adaptive grouping*. In this approach, each patch is associated with its own group, with the center point $\boldsymbol{r}_m$ chosen to minimize the term $|\boldsymbol{r}_m - \boldsymbol{r}|$ in (8). D is then found by the maximum attained value of $2|\boldsymbol{r}_m - \boldsymbol{r}|$, and the sampling rate is determined from (6). In this way, the sampling rate is optimized for each patch, and the basis function patterns are stored at the coarsest possible sampling density.

With this adaptive grouping, (10) is changed to

$$\overline{\overline{Z}}_{j,i} = \kappa \sum_{p=1}^{K} w_p \boldsymbol{V}^*_{j\bar{m}}(k, \hat{\boldsymbol{k}}\bar{p}) \cdot \left(W^T e^{-jk\hat{\boldsymbol{k}}\cdot\boldsymbol{r}_{\bar{m}m}} \cdot T_L(k, \hat{\boldsymbol{k}}_p, \boldsymbol{r}_{mm'}) e^{-jk\hat{\boldsymbol{k}}\cdot\boldsymbol{r}_{m'\bar{m}'}} W \boldsymbol{V}_{i\bar{m}'}(k, \hat{\boldsymbol{k}}\bar{p}) \right), \tag{12}$$

where the notation $\bar{m}$ refers to a group at the adaptive level, and group m is the group at the finest level of the Octree containing $\bar{m}$. W is an interpolation matrix, designed to increase the sampling density of the basis function patterns to that of the translator, such that $W \in \mathbb{R}^{K\times\bar{K}}$, where $\bar{K}$ is the number of plane wave directions used in group $\bar{m}$. Comparing (10) and (12), we can express adaptive grouping as an expansion of the basis function pattern $\boldsymbol{V}_{im'}$ as

$$\boldsymbol{V}_{im'} = e^{-jk\hat{\boldsymbol{k}}\cdot\boldsymbol{r}_{m'\bar{m}'}} W \boldsymbol{V}_{i\bar{m}'}, \tag{13}$$

which, aside from the controllable interpolation error, is exact.

We stress that there are no translations done on the adaptive grouping level, and therefore the near-matrix $\overline{\overline{Z}}_{\text{near}}$ is not based on the adaptive level. Basing $\overline{\overline{Z}}_{\text{near}}$ on the adaptive level would yield a smaller matrix, but this would imply that separate translators would have to be computed for each adaptive group interaction due to the adaptive group center. Without this possibility of reusing translators, which is perhaps the greatest strength of the Octree used with the MLFMM, the memory requirements for the translators, as well as the additional work in translation on the adaptive level, would impair the performance. Another advantage in using the larger Octree groups for the translation is that (5) is more numerically stable for larger groups due to the so-called subwavelength breakdown [11].

In a practical implementation, if each adaptive group has a unique diameter, and thus a unique sampling rate, this would require a significant amount of auxiliary data, in particular the interpolation matrix W for each group. Therefore, our implementation uses a number of specifically allowed sizes, and categorizes each adaptive group into those. Note that only the sampling rate is affected by this categorization, not the center of the adaptive group. For fairly uniform scatterers, only two or three possible sizes are needed, while strongly nonuniform scatterers need a few more. As an estimate for the number of allowed group sizes $N_{\bar{m}}$, we use

$$N_{\bar{m}} = \left\lceil \frac{\max_{\bar{m}} D_{\bar{m}}}{\min_{\bar{m}} D_{\bar{m}}} \right\rceil, \tag{14}$$

where $\bar{m}$ runs through the adaptive groups, and $D_{\bar{m}}$ is the diameter of group $\bar{m}$. We stress that the setup time for the adaptive grouping is insignificant, countable in milliseconds.

The adaptive grouping does not affect the number of nonzeros in the near-matrix $\overline{\overline{Z}}_{\text{near}}$. To reduce the memory required for $\overline{\overline{Z}}_{\text{near}}$, a locally extended Octree grouping can be implemented. This means that l in (11) is modified to equal the largest sidelength of any quad in the group under consideration only, rather than considering all quads in the mesh. Thus, if the mesh is locally very fine, the Octree will locally have additional levels compared to regions with a coarser mesh. Figure 2 provides a small 2-D illustration of a locally extended Octree grouping.

A locally extended Octree was discussed in [12], but was used as a way to reduce the size of the basis function patterns only, not to reduce the memory required for $\overline{\overline{Z}}_{\text{near}}$, as translations on the extended levels was not performed. Further, the

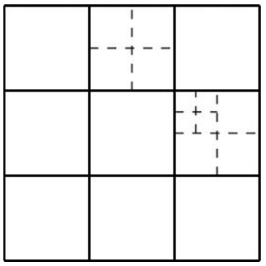

Figure 2 2-D illustration of an Octree grouping using locally extended levels. The solid lines indicate the finest level achieved using the standard Octree grouping. The dashed lines indicate regions where the Octree has been locally refined due to small patches being present in the groups.

focus was not on irregular meshes, so neither the approach nor the results can be compared with the present article.

4. NUMERICAL RESULTS

The first example involves a perfectly electrically conducting (PEC) sphere, designed to illustrate that even for uniformly meshed scatterers, it is beneficial to apply the adaptive grouping, particularly if the group size on the finest level of the Octree is much larger than the patch size. It further illustrates that there is no loss of accuracy from the adaptive grouping.

The second example concerns an irregularly meshed circular PEC plate with several small holes, designed to represent mounting holes. While we stress that these holes are so small that they should not be considered in the electromagnetic representation of the problem, it is fairly common in structures based on CAD (computer-aided-design) to have such features.

The results are based on the implementation detailed in [13], but the implementation does not utilize the storage of basis functions using spherical harmonics expansions (SHEs) [14], as we want to isolate the effects of using adaptive grouping compared to standard Octree grouping at the finest level. However, these two techniques (adaptive grouping and SHE) can easily be combined, and their combination allows use of the SHE to reduce the computational cost of adaptive grouping. We use Lagrange interpolators to step between the sampling rates of the levels. When discussing total memory, we include the memory needed to store the entire MLFMM structure, including near-matrix, basis function patterns etc., as well as minor temporary data, including that needed for interpolation matrices in the adaptive grouping. Throughout, the accuracy setting $\beta = 3$ is used in (6). The error is computed as the relative RMS (root mean square):

$$\text{Relative RMS} = \sqrt{\frac{\sum_{i=1}^{N_s} \left(|\boldsymbol{E}_{i,\text{ref}} - \boldsymbol{E}_{i,\text{cal}}|\right)^2}{\sum_{i=1}^{N_s} |\boldsymbol{E}_{i,\text{ref}}|^2}}, \tag{15}$$

where $\boldsymbol{E}_{i,\text{ref}}$ and $\boldsymbol{E}_{i,\text{cal}}$ denote the reference and calculated electric fields at the ith sample point, respectively, and N_s is the number of samples.

4.1. Sphere

We consider an $\hat{\boldsymbol{x}}$-polarized plane wave at 10 GHz, propagating in the $+\hat{z}$ direction, incident on a 1-m PEC sphere centered at the origin of the co-ordinate system. Using fourth-order basis functions, we vary the sidelength of the patches between 0.9λ and 1.3λ for the fairly uniformly meshed structure, and use the CFIE (3) with α=0.5 to solve the problem, requiring between 3,22,752 and 6,68,352 unknowns. Figure 3 shows the memory consumption as function of the RMS, illustrating the unfortunate property of the Octree grouping to have a very complicated dependence between memory and RMS. In particular, for the scenario $D_q/2 < l \ll D_q$, where l is the largest sidelength in the mesh and q is the finest level, the standard Octree grouping results in extreme memory consumption for the basis function patterns, visible as a peak Figure 3. The adaptive grouping does not have this problem for the basis function patterns, though we can still see the effects through the memory used for the near-matrix. We further see that including the locally extended Octree only has an effect at a single point, further smoothing out the "hump" when the discretization is getting close to allowing an additional level in the Octree.

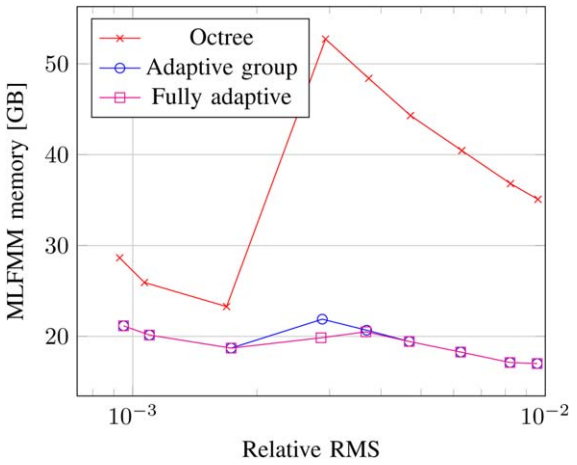

Figure 3 Memory for the entire MLFMM structure, as a function of the accuracy, comparing the traditional Octree grouping at the finest level, using adaptive grouping only, and using adaptive grouping as well as the locally extended Octree (fully adaptive). The RMS is increased by increasing the patch length. [Color figure can be viewed in the online issue, which is available at wileyonlinelibrary.com]

Figure 4 illustrates the time spent per matrix-vector product. We see a modest increase from using the adaptive grouping due to the extra interpolation step. However, particularly for higher-order discretizations, where there are relatively few groups at the finest level, and thus fewer interpolation steps, this will be negligible compared to the significant reduction in memory. Thus, we can conclude that even for uniformly meshed scatterers, there is a very significant potential memory reduction to be achieved using adaptive grouping at the cost of a modest increase in computation time.

4.2. Circular plate with holes

We now consider an $\hat{\boldsymbol{x}}$-polarized plane wave at 300MHz , propagating along $-\hat{z}$, incident on a 36 m diameter circular plate, centered at the origin and positioned in the xy-plane. The plate has nine square mounting holes, each with a sidelength of 0.1λ, placed in a cross around the center. The meshing of this surface with quadrilaterals using sidelengths between 0.1λ and 1.28λ is shown in Figure 5.

The discretization yields $N = 51491$ unknowns, with polynomials up to seventh-order being used on the largest patches. The default Octree grouping yields a fairly poor grouping, with a sidelength at the finest level of 2.25λ. This results in 3.79 GB of total memory. Using the adaptive grouping and locally

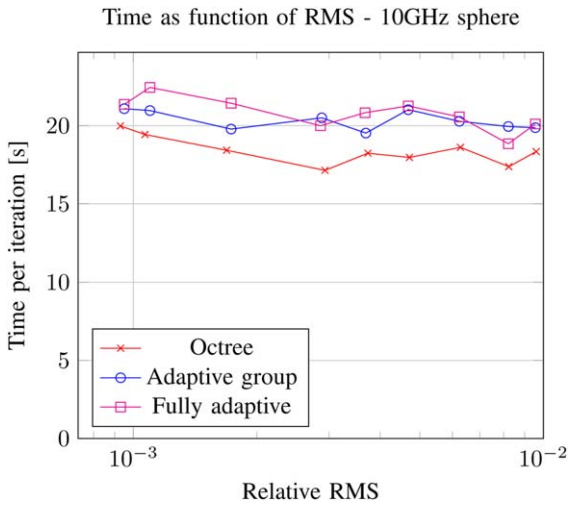

Figure 4 Time per matrix-vector product, as a function of the accuracy, comparing the traditional Octree grouping at the finest level, using adaptive grouping only, and using adaptive grouping as well as the locally extended Octree (fully adaptive). We note that the differences between the adaptive grouping only and the "fully adaptive" approach are primarily due to inaccuracies in the timings. [Color figure can be viewed in the online issue, which is available at wileyonlinelibrary.com]

extended Octree, the memory is reduced to less than a sixth, 623 MB, while the time per matrix-vector product is increased by roughly 8%. The memory for the basis function patterns alone is reduced from 3.1 GB to 426 MB, a factor of 7.5. We note that with adaptive grouping, but without the locally extended Octree, the total memory required would have been 1.09 GB, so for this strongly nonuniform mesh, the locally extended Octree is effective.

Figure 6 shows the scattered fields from each of the two techniques, further demonstrating that the proposed adaptive approach, with both adaptive grouping and a locally extended Octree, yields the same result as the standard Octree grouping.

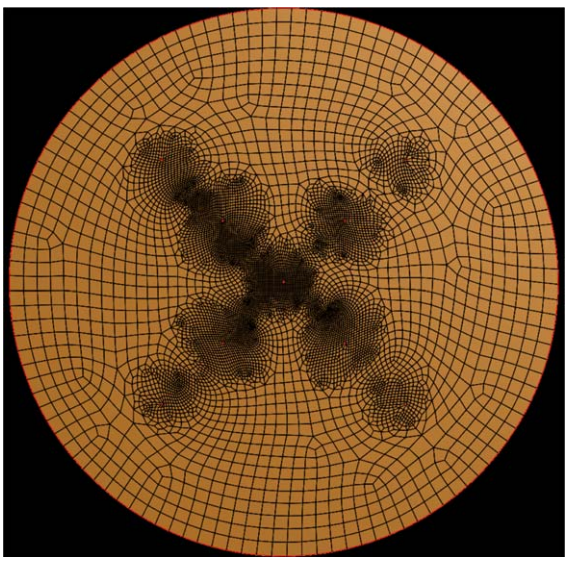

Figure 5 Circular plate with nine $0.1\lambda \times 0.1\lambda$ mounting holes. [Color figure can be viewed in the online issue, which is available at wileyonlinelibrary.com]

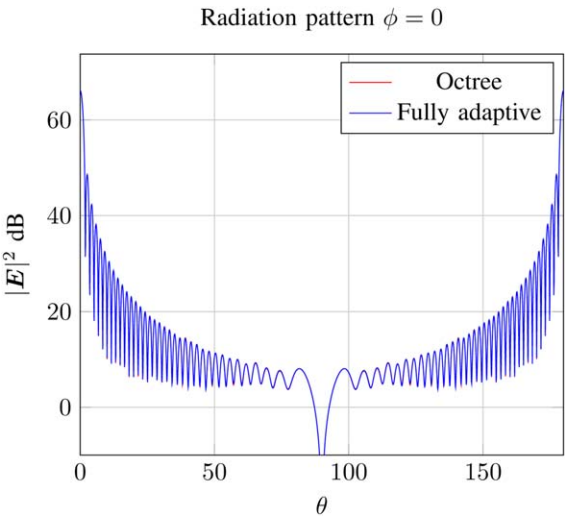

Figure 6 The scattered far-field for a circular plate with holes, for ϕ=0. Both the results from using Octree grouping and the adaptive grouping are shown, demonstrating that there is no loss of accuracy. [Color figure can be viewed in the online issue, which is available at wileyonlinelibrary.com]

5. CONCLUSIONS

Our results demonstrate that the proposed adaptive grouping approach should be included in modern implementations of MLFMM, particularly when using a higher-order discretization with larger patch sidelengths. Further, for strongly nonuniform meshes, a locally extended Octree should also be implemented. For a modest increase in computation time, the reduction in memory obtained with these methods is significant and the implementation is simple.

REFERENCES

1. V. Rokhlin, Diagonal Forms of Translation Operators for Helmholtz Equation in Three Dimensions, Technical Report, March 1992.
2. C.-C. Lu and W.C. Chew, A multilevel algorithm for solving a boundary integral equation of wave scattering, Microwave and Optical Technology Lett 7 (1994), 466–470.
3. R. Coifman, V. Rokhlin, and S. M. Wandzura, The fast multipole method for the wave equation: A pedestrian prescription, IEEE Antennas Propagat Mag 35 (1993), 7–12.
4. J.M. Song and W.C. Chew, Multilevel fast-multipole algorithm for solving combined field integral equations of electromagnetic scattering, Microwave Optical Technol Lett 10 (1995), 14–19.
5. D. Meagher, Geometric modeling using octree encoding, Comput Graph Image Process 19 (1982), 129–147.
6. S. Velamparambil, W.C. Chew, and J. Song, 10 million unknowns: Is it that big? IEEE Antennas Propagat Mag 45 (2003), 43–58.
7. J.R. Mautz and R.F. Harrington, H-field, E-field, combined field solutions for bodies of revolution, IEEE Antennas Propagat Soc Newslett 19 (1977), 7.
8. J. Song and W.C. Chew, Error analysis for the truncation of multipole expansion of vector green's functions, IEEE Microwave Wireless Compon Lett 11 (2001), 311–313.
9. R.F. Harrington, Matrix methods for field problems, Proc IEEE 55 (1967), 136–149.
10. S. Koc, J.M. Song, and W.C. Chew, Error analysis for the numerical evaluation of the diagonal forms of the scalar spherical addition theorem, SIAM J Num Anal 36 (1999), 906–921.
11. M. L. Hastriter, S. Ohnuki, and W. C. Chew, Error control of the translation operator in 3D MLFMA, Microwave Opt Technol Lett 37 (2003), 184–188.

12. X.-M. Pan, L. Cai, and X.-Q. Sheng, An efficient high order multilevel fast multipole algorithm for electromagnetic scattering analysis, Prog Electromagn Res 126 (2012), 85–100.
13. O. Borries, P. Meincke, E. Jørgensen, and P.C. Hansen, Multi-level fast multipole method for higher-order discretizations, IEEE Trans Antennas Propagat 62 (2014), 3119–3129.
14. T. F. Eibert, A diagonalized multilevel fast multipole method with spherical harmonics expansion of the k-space Integrals, IEEE Transactions on Antennas and Propagation, 53 2005, 814–817.

A DOWN-CONVERSION MIXER USING 90-NM CMOS PROCESS FOR 60-GHZ APPLICATIONS

Chia-Yang Huang, Yu-Hsin Chang, and Yen-Chung Chiang
Department of Electrical Engineering, National Chung Hsing University, Taichung, 40227, Taiwan, R.O.C; Corresponding author: ycchiang1970@nchu.edu.tw

Received 4 March 2014

ABSTRACT: *This article proposes a double-balanced 60- to 12-GHz down-conversion mixer fabricated in the 90-nm CMOS process. The proposed mixer has a 5.825 dB measured conversion gain and 13–16 dB noise figure. The input P_{1dB} of the mixer is −4.4 dBm and the measured LO-IF, LO-RF, and RF-IF isolations are above 42, 44, and 41.5 dB, respectively.* © 2014 Wiley Periodicals, Inc. Microwave Opt Technol Lett 56:2456–2458, 2014; View this article online at wileyonlinelibrary.com. DOI 10.1002/mop.28610

Key words: *60-GHz band; CMOS process technology; double-balanced topology; down-conversion mixer*

1. INTRODUCTION

Owing to the rapid growing demand on the high data rate wireless communication, RF bands within 10 GHz for existing wireless systems become too crowded and cannot satisfy people's requirement. Recently, systems using the 60 GHz band have drawn increasing interests because of its 7-GHz unlicensed bandwidth [1] and other channel characteristics including good data security and low inference. Just as other wireless communication systems, the RF front end plays an important role in the performance of whole system. The mixer that performs frequency conversion is an essential component in the RF front end. Mixers for 60 GHz systems can be realized by passive mixers [2,3] or active mixers [4–8]. The passive mixers do not consume power and have better linearity performance but they suffer from the drawback of no gain. Gilbert cell architectures [4–6] and gate-pumped mixers [7,8] are in the category of active mixers to provide conversion gains (CGs). Although the Gilbert cell is the most common topology for mixer design, the CG may be limited by the loss via the parasitic capacitance between the transconductance (G_m) stage and the switch stage and by the operation speed of the switch devices. In the conventional gate-pumped topology, the RF and LO signals are combined by some kind of passive coupling structure, then the combined signals are fed into the gate terminal of the CMOS device and the IF signal is generated by the nonlinearity of the device. The port-to-port isolations of such kind of mixers significantly depend on the design of the coupling structure which usually occupies a large area.

In this article, we utilize the nonlinearity effect of the devices via the voltage difference between the gate terminal and the source terminal and design a 60- to 12-GHz mixer using the TSMC 90-nm CMOS process technology. The design considerations are presented in Section 2, measured results of the proposed mixer are shown in Section 3, and then a simple conclusion is drawn in Section 4.

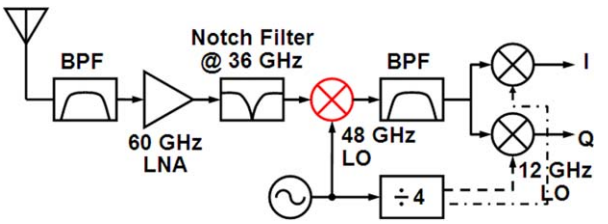

Figure 1 System diagram of a super-heterodyne receiver for 60 GHz band applications. [Color figure can be viewed in the online issue, which is available at wileyonlinelibrary.com]

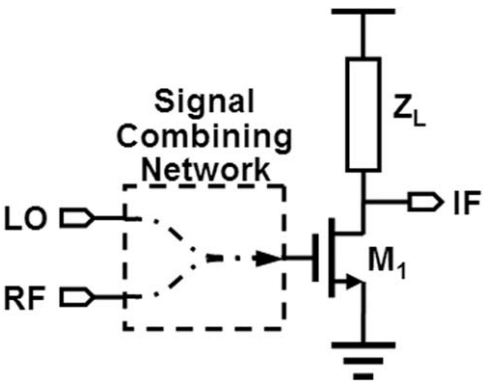

Figure 2 Schematic of a simplified gate-pumped mixer

2. CIRCUIT DESIGN

Due to the frequency planning consideration of the system, we adopt the super-heterodyne architecture as shown in Figure 1 which is similar to that proposed in [9]. The proposed mixer is the RF mixer which down-converts the 60 GHz signal to the 12-GHz IF band. As it is the second stage (excluding the filters before and after the LNA (low noise amplifier)) of the whole system, the major objectives to achieve are sufficient CG, low noise figure (NF), and good linearity (P_{1dB} or IIP3).

Figure 2 shows a simplified circuit of the gate-pumped mixer. As indicated in the previous section, the RF and LO signals are combined by some kind of coupling structure and the combined signal is fed into the gate terminal of the CMOS device M_1. Due to the nonlinear effect of the active device, a current with the required

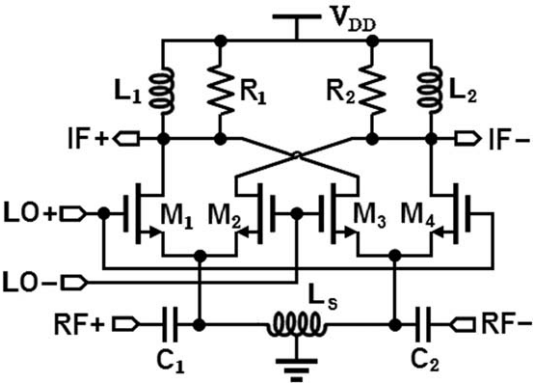

Figure 3 Schematic of the proposed 60- to 12-GHz mixer